Multiphosphorylated Molecule for Buried Interface Regulation of Inverted Perovskite Solar Cells in Two-step Process

Shizi Luo,[ab] Zhuoneng Bi,[b] Liyao Xiong,[ab] Tongjun Zheng,[ab] Xiaochun Wei,[c] Youliang Nie,[ab] Biniyam Zemene Taye,[abd] Jing Zhou,[b] Haider Ali Tauqeer,[ab] Lavrenty Gutsev,*[e] Andrey Vasenko,[f] Gennady Gutsev,[g] Oleg Prezhdo,[h] Huangzhong Yu[c] and Xueqing Xu*[ab]*

[a] School of Energy Science and Engineering, University of Science and Technology of China, Hefei, 230026, P.R. China

[b] Guangzhou Institute of Energy Conversion, Chinese Academy of Sciences
CAS Key Laboratory of Renewable Energy
Guangdong Provincial Key Laboratory of Renewable Energy

[c] School of Physics and Optoelectronics, South China University of Technology, 510640 Guangzhou, China

[d] Faculty of Electrical and Computer Engineering, Bahir Dar Institute of Technology, Bahir Dar University, Bahir Dar, P.O. Box 26 Ethiopia

[e] Institute for Micromanufacturing, Louisiana Tech University, Ruston, LA 71272, United States

[f] HSE University, 101000 Moscow, Russia.

[g] Department of Physics, Florida A&M 711 University, Tallahassee, Florida 32307, the United States

[h] Department of Chemistry and Chemical Biology, University of New Mexico, Albuquerque, NM 87106, the United States

* Corresponding authors.

E-mail addresses:

xuxq@ms.giec.ac.cn (X. Xu);

Keywords: Multiphosphorylated molecules, Optimizing SAM, Buried interface regulation, Two-step process, Inverted perovskite solar cells

1. Materials

Dimethylformamide (DMF, >99%), dimethyl sulfoxide (DMSO, >99.5%), chlorobenzene (CB, anhydrous, 99.8%) were purchased from Sigma-Aldrich. Isopropyl alcohol (IPA, anhydrous, 99.8%) was purchased from Acros. The NiO_x powder, lead iodide (PbI_2, 99.99%) and lead bromide ($PbBr_2$) were purchased from Advanced Election Technology Co., Ltd. CsI, [6,6]-Phenyl-C_{61}-butyric acid methyl ester (PCBM), 2,9-Dimethyl-4,7-diphenyl-1,10-phenanthroline (BCP), methylammonium chloride (MACl), formamidinium iodide (FAI) and methylammonium bromide (MABr) were purchased from Xi'an Yuri Solar Co., Ltd. [4-(3,6-Dimethyl-9H-carbazol-9-yl)butyl]phosphonic Acid (Me-4PACz) was purchased from was purchased from Acros (TCI). Ethylenediamine tetramethylenephosphonic acid (EAPA) was purchased from Aladdin.

2. Fabrication of Rigid Small-Area PSCs

The ITO-coated glass substrates (purchased from Wuhan Lattice Solar Energy Technology Co. LTD.) were ultrasonically cleaned with soap solution, deionized water, ethanol and isopropyl alcohol each for 20 min, respectively, and then dried under a stream of nitrogen. The pre-cleaned ITO/glass substrates were treated with UV-Ozone (UVO) for 15 min to remove the organic residue. The NiO_x nanoparticle solution (10 mg/mL) was spin-coated onto the ITO/glass substrates at 2000 rpm for 30 s and annealed for 10 min at 150℃, then quickly transferred to a glove box. Me-4PACz (0.5 mg/mL in ethanol) was spin-coated on NiO_x at 4000 rpm for 30 s, annealed for 10 min at 100℃ and cooled for 5 min. Subsequently, 0.05, 0.1, and 0.2 mg EAPA powder dissolved in 1 mL DMSO respectively, were spin-coated on Me-4PACz at 5000 rpm for 30 s before annealed for 10 min at 100℃.

The preparation of perovskite with a bandgap of 1.56 eV in N_2: PbI_2 powder (1.5 M), CsI powder (0.06 M) and RbCl (0.015 M) in mixed solvent (DMF and DMSO with volume ratio of 9:1) was dropped onto the HTL and spin-coated at 2500 rpm for 30 s, then annealed for 1 min at 70℃. Organic salt solution (FAI/MAI/MACl (90:9:9 mg) in

1 mL IPA was dynamically dropped onto the PbI_2 film after 5 s of the process starting at 3500 rpm for 35 s, and then annealed for 50 min at 100℃.

The preparation of perovskite with a bandgap of 1.68 eV in N_2: PbI_2 powder (1.125 M), $PbBr_2$ powder (0.375 M), CsI powder (0.06 M) and RbCl (0.015 M) in mixed solvent (DMF and DMSO with volume ratio of 9:1) was dropped onto the HTL and spin-coated at 2500 rpm for 30 s, then annealed for 1 min at 70℃. Organic salts solution (FAI/MABr/MACl (90:9:9 mg) in 1 mL IPA was dynamically dropped onto the PbX_2 film after 5 s of the process starting at 3500 rpm for 35 s, and then annealed for 30 min at 100℃.

For post-treatment, 1 mg/mL PEAI in IPA solvent was dynamically spin-coated onto the perovskite surface with 4000 rpm for 30 s, and then annealed for 5 min at 100℃. Next, 20 mg/mL PCBM in CB and 0.5 mg/mL BCP in IPA was spin coated at 2000 rpm and 4000 rpm for 30 s, respectively. Finally, the Ag top electrode (100 nm) was deposited by thermal evaporation in vacuum through a shadow mask defining the device active area as 0.048 cm^2.

The method for fabricating devices without Me-4PACz: Apart from not spin-coating Me-4PACz, the fabrication methods for other functional layers and devices with Me-4PACz are the same.

The blade-coating preparation method for the SAM layer: SAM precursor deposition was performed in dry box (R.H. 10% ~ 20%). The SAM precursor solution (25 μL) was coated by using doctor blade coater (Zehntner ZAA 2300) at the substrate temperature of 25°C. The gap between the blade and the substrate was 150 μm and the blade speed were 5 mm/s. The wet films were dried by N_2 blowing and then annealed at 100 ℃ for 10 min to dry films. The concentration of the SAM layer is the same as that of the spin-coating process, and the preparation methods for other functional layers are also the same as those of the spin-coating process.

The perovskite films fabricated using the conventional antisolvent-assisted annealing method: $Cs_{0.05}(FA_{0.95}MA_{0.05})_{0.95}Pb(I_{0.95}Br_{0.05})_3$ perovskite precursor solution was prepared by mixing 6.7 mg MABr, 8.8 mg MACl, 18.2 mg CsI, 196.1 mg FAI, 22 mg $PbBr_2$ and 572 mg PbI_2 in 865 uL mixed solvent of DMF: DMSO = 4:1 v/v and

stirred at 60℃ for 1 h. Then as-prepared perovskite precursor solution was spin-coated onto SAM layers with speed of 1000 rpm for 5 s and 4000 rpm for 30 s. The wet film was treated by drop-casting 120 uL ethyl acetate during the last 15 s of the spinning process and subsequently annealed at 100°C for 50 min to obtain perovskite films with a bandgap of 1.56 eV. The preparation methods for other functional layers are also the same as those used in the two-step process for fabricating the device.

3. Characterizations

The perovskite films were characterized by X-ray photoelectron spectroscopy (XPS, ESCALAB 250Xi, Thermo Scientific K-Alpha). Ultraviolet photoelectron spectra (UPS) were also measured by Thermo Scientific ESCALAB 250Xi, with the HeI (21.22 eV) emission line employed for excitation. The surface microstructure of perovskite films and the cross-sectional images of PSCs were obtained using SU-70 high-resolution analytical SEM (Hitachi, Japan). PL and TRPL spectra of perovskite films were obtained using Edinburgh fluorescence spectrometer (FLS980). The X-ray diffraction (XRD) patterns of perovskite films were obtained using X'Pert PRO MPD X-Ray diffractometer with Cu Kα irradiation at a scan rate (2θ) of 0.0167 ° S^{-1}. For *J-V* measurements, the intensity of the light was 100 mW cm^{-2} (simulated AM 1.5 G) provided by ABET Sun 3000 solar simulator and calibrated by a standard silicon reference cell. Grazing incidence X-ray diffraction (GIXRD) was performed using Rigaku SmartLab. Atomic force microscopy (AFM) measurements were performed by Bruker Multimode. The *J-V* curves, space charge-limited current (SCLC) for the solar cells were performed using Autolab TYPE II electrochemical work station. The external quantum efficiency (EQE) spectra of the solar cells were obtained using QTest Hifinity 5 (Crowntech, USA). The operational stability of the PSCs was studied at maximum power point tracking (MPPT) using a 100 mW cm^{-2} white LED lamp (Suzhou D&R Instrument Co., Ltd.) in an N_2-filled glove box. Peak force quantitative nanomechanical atomic force microscopy (PFQNM-AFM) measurements were carried out using a Bruker Multimode 8 at Shiyanjia Lab.

4. Density Functional Theory

The Vienna Ab initio Simulation Package (VASP) software suite [1] was utilized to perform surface-based calculations. We employed a PBE functional [2] with an added D3 dispersion corrections.[3] This is a commonly utilized GGA+D3 method which benefits from a fortuitous error cancellation between self-interaction interactions and the absence of Spin-Orbit Coupling (SOC) in SOC-free calculations. As a result, this method provides unusually accurate band gap predictions at the GGA level. Also, it was shown to provide reasonable agreement between computed and experimental lattice constants of $CsPbI_3$ and $RbPbI_3$ [4] and to offer a reasonable compromise when calculating defect formation energies.[5] As in our previous work, the α-FAPbI3 surface was oriented along the Miller index (100) and we chose two symmetrical terminations to represent two possibilities: one where the PbI_2-rich surface exposed and another one where the FAI-rich surface is exposed. In this work, we refer to the (100) direction as the "z-axis" for clarity. Full relaxation of atomic positions and lattice constants was allowed with the only constraint that the constant cell volume is maintained (ISIF=4 in VASP). We used a relatively large 3 × 3 × 5 supercell which we prepared by using the Atomic Simulation Environment (ASE). To ensure that mirror images do not interact, we included a vacuum layer of 20 Å along the z-axis. We replicated a similar scheme for simulating the passivation of a rocksalt NiO (110) surface. Previously,[6] we used the Zurr-McGill algorithm to reveal that this surface is well-matched with the (100) surface of α-FAPI. In particular, a relatively large 9.31x11.91 $Å^2$ surface slab, which is 5 layers deep, was prepared with symmetrical terminations, where two terminations types were considered: O-rich and O-medium. As with the perovskite calculations, 20 Å of vacuum were added above the z-axis which is the (110) direction in this case. Non-spherical contributions were also added to the gradient within the PAW spheres, since it was previously shown that they enhance significantly the accuracy of simulated observables of the perovskite oxides. [7]

The FAPI calculations were performed using projector augmented-wave (PAW) pseudopotentials [8, 9] and a 2x2x1 Monkhurst-Pack mesh with a plane-wave energy

cutoff of 520 eV. This choice is justified by the fact that the overall plane-wave energy cutoff ought to be about 30% larger than the largest atomic cutoff of the pseudopotentials used to obtain high quality VASP results. In the present case, the largest values are 400 eV for C and O; therefore, the VASP cutoff was 520 eV. The results of calculations on the EAPA and Me-4PACz adsorption on the FAI-Rich and PbI_2-Rich (100) α-FAPI surfaces are presented in Figure 2c.

In the case of NiO, we used a 3×3×1 *k*-grid and included in computations the onsite Hubbard constant via the U-J Dudarev Scheme [10] where U = 4.6 eV[11] and J = 0.0 eV. It is notable that the Materials Project manual [12] recommends U = 6.2 eV but the geometry does not significantly change if any of these two U values are used.

Adsorption energies E_{ads} were calculated using the formula:

$$E_{ads}(D^q) = E_{\overline{surf}}(D^q) - E_{surf}(D^q) - E_{pass} \qquad (2)$$
$$\overline{pass}$$

where $E_{surf/pass}$ is the energy of the passivator plus the surface while E_{surf} and E_{pass} are the energies of the surface and passivator, respectively, and D^q indicates a defect type. We considered the pristine surfaces for PbI_2-rich (100) α-FAPI, a FAI-rich (100) α-FAPI surfaces, an O-Rich (110) NiO rocksalt surface and an O-Medium NiO rocksalt surfaces. The passivators considered were Me-4PACz and EAPA. In the case of NiO, we have previously performed ab initio MD calculations and thus knew that at least one proton leaves the phosphonate moiety and adheres to the nickel-oxide surface. Our tests indicated that this is also valid for EAPA and, hence, the exceptionally high adsorption energies reported in the main text are likely related to this factor.

We performed gas phase (Figs S4 and S5) calculations of EAPA, Me4PACz and interactions between them using GAUSSIAN 16c software [13] and visualized the results obtained with Chemcraft. The hybrid B3LYP functional and a 6-31G* basis set was employed, along, D3 dispersion corrections were included.

5. Classical Molecular Dynamics

As a variant of classical Molecular Dynamics, we used the LAMMPS molecular dynamics simulator.[14] Since we discussed in detail how to apply this appriach in our previous work,[6] we will shortly summarize the method and discuss the changes made. The custom code discussed below is now freely available on Github: https://github.com/lgutsev/NiO_MD_Passivation/

To start with, we generated the OPLS-AA parameters via the LigParGen server.[15] In addition, we further modified the forcefields as described by Metzger et al.[16] This scheme works quite well for Me4PACz; but given that EAPA is essentially a multidentate phosphonate, we made further changes to its forcefield. In particular, we reduced the stiffness of the phosphonate heads by reducing the bond coefficients pertaining to P–O(H) and P=O as well as the C-P-O angle coefficient. Additionally, we also loosened the LJ repulsion of the hydroxyl oxygens to prevent artificial interactions involving the hydroxyl hydrogens. Finally, we also reduced the net P–P interaction potential. These changes allowed for reasonable description of interactions between Me-4PACz and EAPA while retaining numerical stability of the LAMMPs calculation. For more realistic charge descriptions, we also calculated and utilized electrostatic potential-derived charges according to the CHelp scheme [17] in the Gaussian16 package of programs [13] with an improved B3LYP/6-311G* method. For all calculations we utilized 0.5 scaling of the Coulomb 1-4 interactions which is widely utilized for OPLS-AA,[18] In the NiO case, we used two forcefields for two different goals:

A NiO Lennard–Jones (LJ) force field was employed to describe nonbonded interactions between the ligand and the NiO surface. The pairwise interaction parameters between each ligand atom and the Ni or O atoms were obtained using the standard geometric mixing rule.For the actual simulation of the corrugated NiO system, we utilized a Buckingham three-parameter forcefield which we previously fitted to closely replicate the atomic distances of a DFT molecular dynamics simulation of the NiO (110) surface.

The values of mixed pair interactions we presently generated are quite similar to our previous values as well as to the values of the 2PACz-SnO_2 mixed pair coefficient values.[19]

A velocity Verlet method was applied to integrate the equations of motion with a time step of 1 femtosecond in the case of NiO passivated with Me-4PACz and a time step of 0.25 femtosecond in the case when EAPA is added. This was necessary since the EAPA is quite flexible and strongly interacts with the Me-4PACz SAM as well as the NiO surface. Isothermal–isobaric conditions were maintained using a Nosé–Hoover thermostat with a time constant of 0.1 ps. To control pressure, a Nosé–Hoover barostat with a damping parameter of 1000 fs was applied, enabling fluctuations of the *x* and *y* lattice constants. The cutoff distances for van der Waals and Coulombic interactions were set to 10.0 Å and 8.0 Å, respectively. Long-range Coulombic interactions were treated using the particle–particle particle–mesh (PPPM) method with an achieved accuracy of 1×10^{-4} (kcal mol^{-1}) Å^{-1}.

The surface was simulated as a corrugated nickel oxide surface. In this case we used a long NiO 12.51 × 4.17 × 4.17 nm^3 supercell and cut a V-shaped wedge down corresponding to two (011) and $(0\bar{1}1)$ cuts along the long *x* direction. The wedge obtained was 8 layers deep with a remaining connecting "lip" (see previous paper [6]) between periodic wedges which was 6 layers wide. Such low miller index surfaces are associated with low surface energies [20] and the surfaces we generated have the particular advantage of not being polar [21] which makes comparison of DFT with the simpler forcefield-based method more straightforward.

The system was modeled as periodic in the *x* and *y* directions and reflective in *z*, with over 100 Å of vacuum above the surface and 15 Å below. To achieve significant coverage of the surface, we utilized a dynamic application method.[5] In short, the passivating Me-4PACz molecules (or passivant plus EAPA) were first allowed to aggregate briefly in the vacuum above the surface, after which a gradually advancing Lennard-Jones 12-6 potential wall pushed the material toward the surface, the pushing was done for 0.1 ps. Once deposition was complete, the system recoiled slightly in the *z*-direction, then stabilized as a recoil-absorbing wall was introduced below the surface to prevent upward bouncing. Following application of the passivant layer, the MD simulation showed only minimal structural rearrangement, indicating that the film

remained largely immobile due to stabilization by its hydrogen-bonded network. Thus, the self-organized configuration present immediately after application is the most representative for subsequent analysis. This procedure was carried out for Me-4PACz alone, in which 180 Me-4PACz molecules were applied, as well as for the 5:1 Me-4PACz: EAPA mixture, which consisted of 180 Me-4PACz molecules and 36 EAPA molecules.

6. Supplementary Note

Note 1. The conductivity (σ) was calculated by the following formula:

$$\sigma = \frac{dA}{R}$$

where R, d and A represent the resistance, the thickness of the top electron transport layer, and the film area.

Note 2. Using the space charge limited current (SCLC) model, the hole mobility of the sample was measured with a pure hole device structure (such as ITO/hole transport layer/Ag structure). The *J-V* curve was fitted using the Mott-Gurney law to calculate the hole mobility.[22, 23] In the SCLC region (typically the higher voltage range), the *J-V* curve was transformed by taking the square root：

$$J = \frac{9}{8}\varepsilon_0\varepsilon_r\mu\frac{(V - V_r - V_{bi})^2}{L^3}$$

At higher voltage levels (in our work, the voltage range is 2.5 - 4 V), the slope *k* was obtained through linear fitting, with $k = \frac{\sqrt{J}}{V}$.

Based on the slope *k* and the known parameters, calculate the hole mobility: $\mu = \frac{8k^2L^3}{9\varepsilon_0\varepsilon_r}$

where *J* is the current density, ε_0 is the vacuum permittivity, ε_r is the dielectric permittivity of the NiO_x/Me-4PACz, *L* is the film thickness, *V* is the applied voltage of the device, V_r is the voltage drop due to the constant resistance and series resistance across the electrodes, V_{bi} is the built-in voltage due to the different work function of the two electrodes, and μ is the hole mobility.

Note 3. The geometric structure at the heterojunction interface between the perovskite and the hole transport layer is determined by the ratio of the GB energy to the heterojunction energy,[24]

$$\frac{\gamma_{GB}}{\gamma_{HI}} = 2\cos(\psi/2)$$

where γ_{GB} is the GB energy, γ_{HI} is the heterojunction interface energy, ψ is the groove angles of the GB, as shown in the legend of Figures 2g, h)

Note 4. Detailed TRPL fitting results were obtained by using a dual exponential decay function model presented by the following equation:

$$I(t) = I_0 + A_1 \exp\left(-\frac{t}{\tau_1}\right) + A_2 \exp\left(-\frac{t}{\tau_2}\right)$$

Note 5. τ_{ave} can be calculated by the equation:

$$\tau_{ave} = \frac{A_1 * \tau_1^{\,2} + A_2 * \tau_2^{\,2}}{A_1 * \tau_1 + A_2 * \tau_2}$$

Note 6. QFLS can be calculated from PLQY by the following formula:

$$QFLS = QFLS_{rad} + k_B T ln(PLQY)$$

Here, $QFLS_{rad}$ is the radiative limit of our semiconducting material, setting the maximum achievable splitting of the quasi-Fermi levels, hence the V_{OC}, in the case of zero nonradiative recombination. K_B is the Boltzmann constant, J_G is the photogenerated current density, and $J_{0,\ rad}$ is the dark state radiative recombination saturation current density.

Note 7. The trap state density for the measurement of space charge limited current was calculated by using the formula:

$$N_t = \frac{2\varepsilon_0 \varepsilon_r V_{TFL}}{qL^2},$$

where ε_0, ε_r, V_{TFL}, q and L represent the vacuum dielectric constant, relative dielectric constant, trap filling limit voltage, fundamental charge, and the perovskite film thickness, respectively.

Note 8. The maximum FF (FF_{max}) without charge transport loss can be calculated through the formulas:

$$v = \frac{qV_{OC}}{nkBT}$$

$$FF_{max} = \frac{v - \ln(v + 0.72)}{v + 1}$$

where q is the elementary charge, n is the ideality factor, k_B is the Boltzmann constant, T is the absolute temperature.

7. Figures and tables

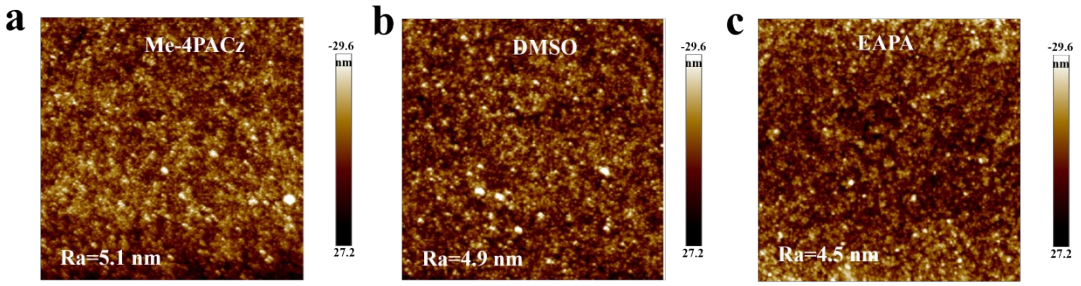

Fig. S1 AFM 2D topography images (5×5 um^2) of (a) ITO/NiO_x/Me-4PACz, (b) ITO/NiO_x/Me-4PACz/DMSO and (c) ITO/NiO_x/Me-4PACz/EAPA structure.

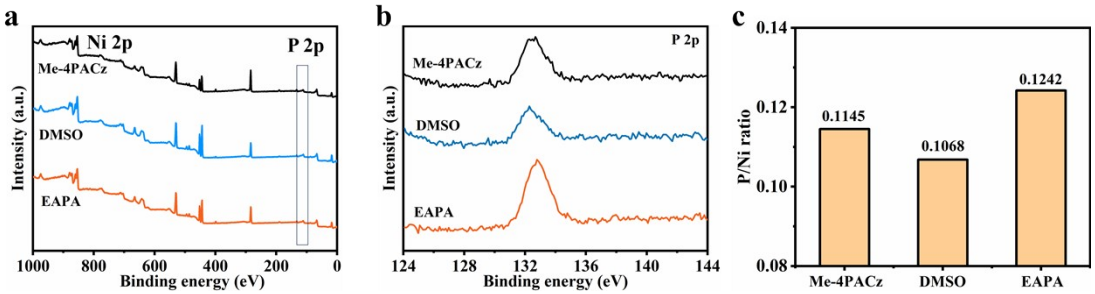

Fig. S2 (a) Survey XPS spectra, (b) P 2p XPS core spectra and (c) P/Ni ratio for the Me-4PACz, DMSO and the EAPA samples, respectively.

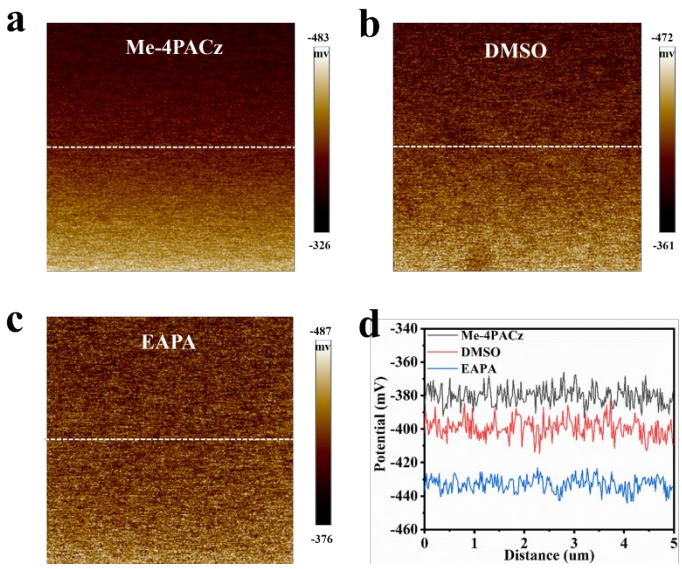

Fig. S3 KPFM images of the (a) ITO/NiO_x/Me-4PACz, (b) ITO/NiO_x/Me-4PACz/DMSO and (c) ITO/NiO_x/Me-4PACz/EAPA, respectively. (d) Surface contact potential difference images of the different substrates.

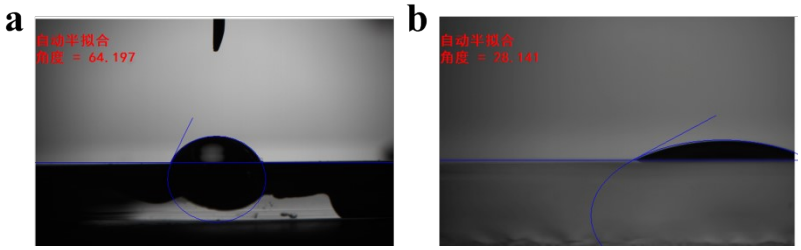

Fig. S4 Water contact angle of (a) ITO/NiO_x/Me-4PACz and (b) ITO/NiO_x/Me-4PACz/EAPA.

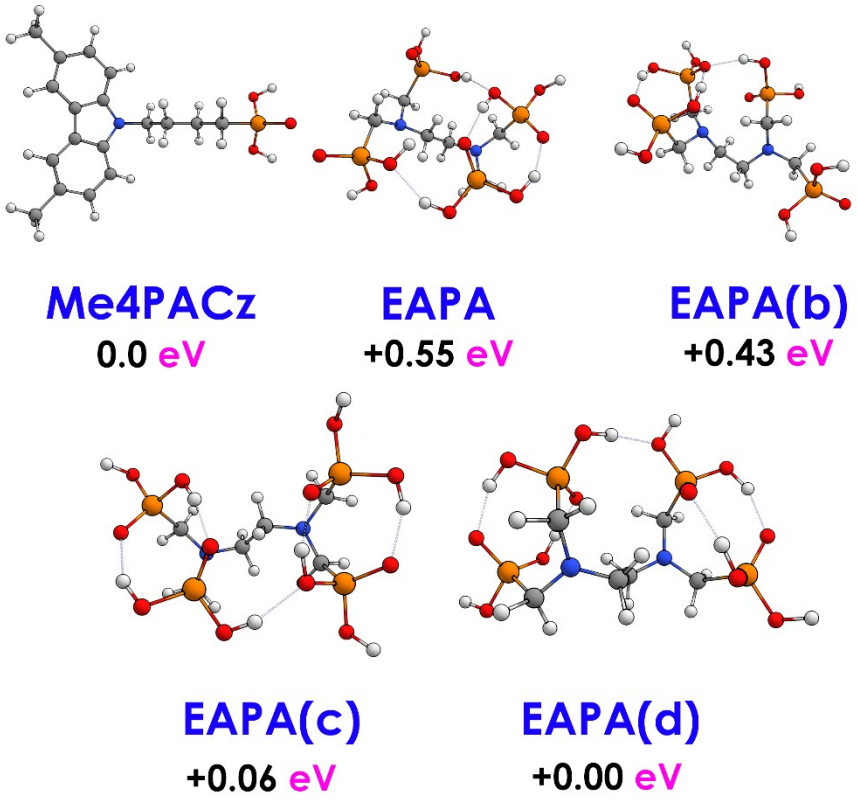

Fig. S5 The optimized B3LYP+D3/6-31G* structures of Me-4PACz and four rotamers of EAPA.

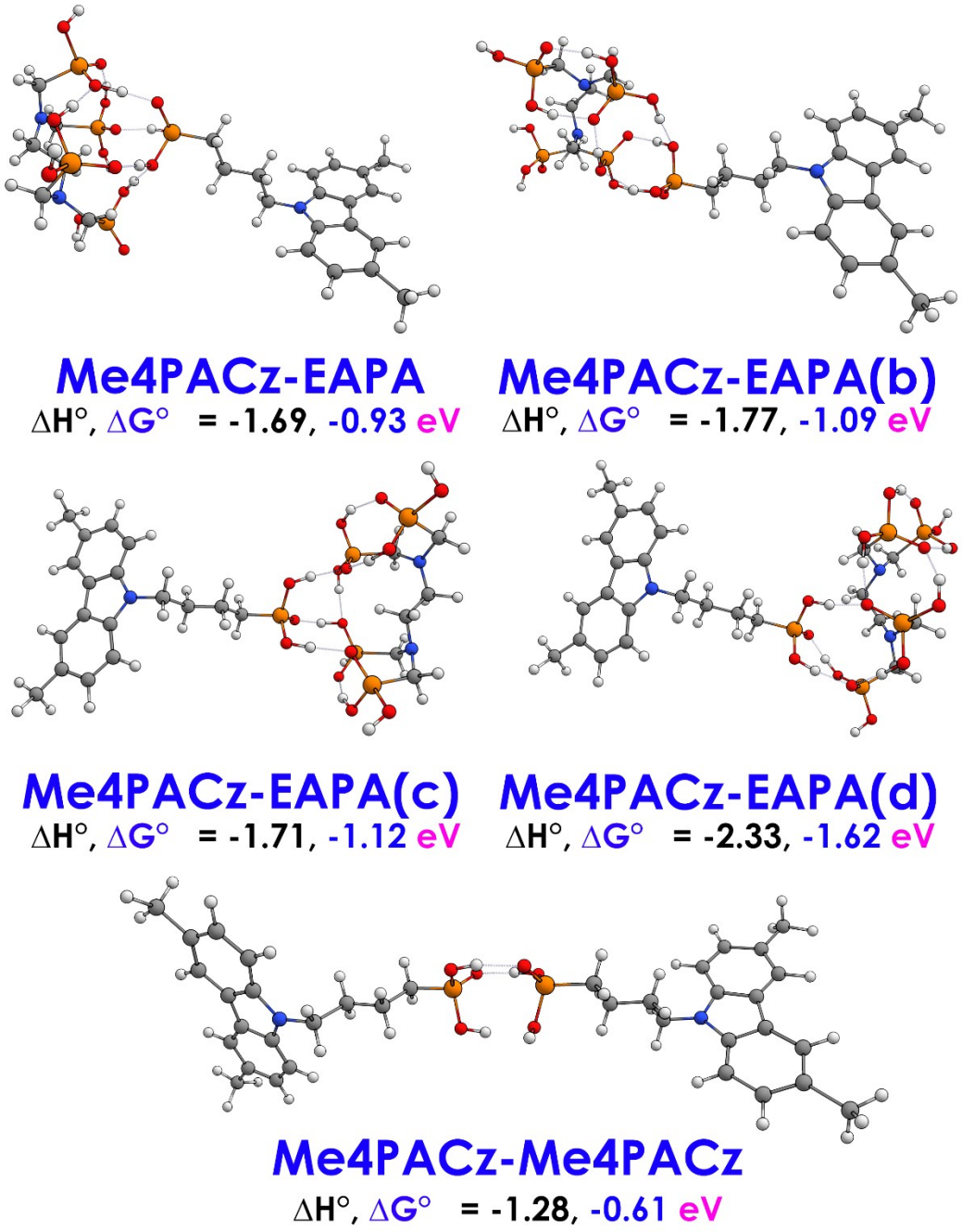

Fig. S6 The geometrical configurations of the Me4PACz interaction with its congener Me4PACz as well as interactions Me4PACz with the four rotamers of EAPA. The presented are also the calculated gas-phase binding enthalpy ($^{\Delta H^\circ}$) and Gibbs free binding energies ($^{\Delta G^\circ}$) of each interaction. The energies are all reported as calculated whereas we report per molecular unit (divided by two) in the main text.

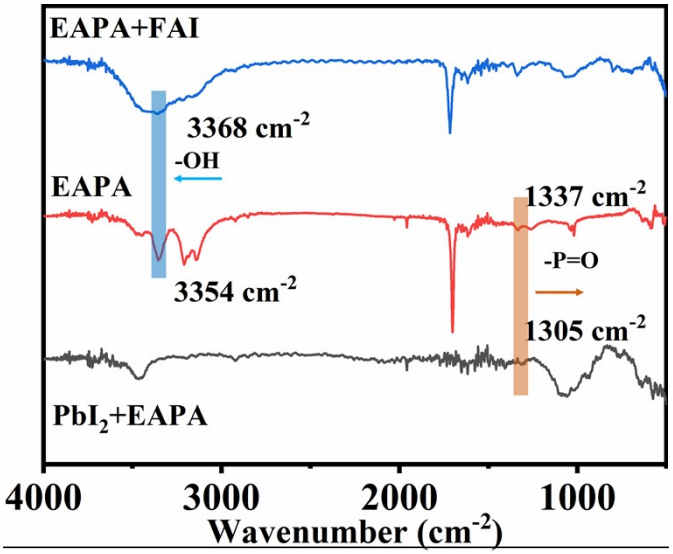

Fig. S7 FTIR spectra of EAPA, EAPA+PbI_2 and EAPA+FAI.

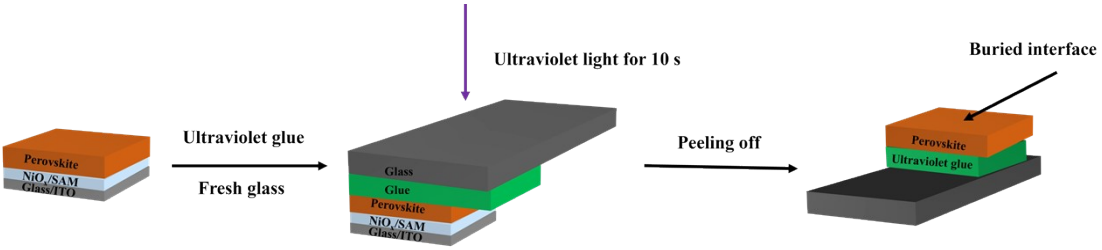

Fig. S8 Using ultraviolet glue to peel off the perovskite film from the NiO_x/SAM/Perovskite structure, thereby exposing the buried interface of the perovskite films.

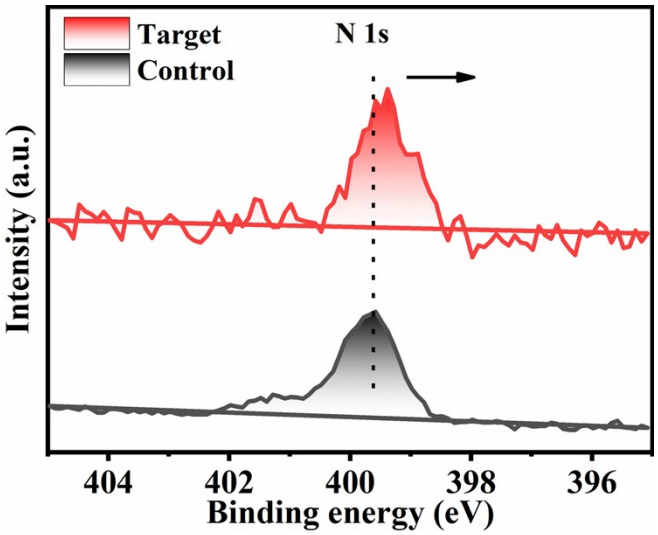

Fig. S9 High-resolution XPS spectra of the corresponding perovskite films featuring N 1s band.

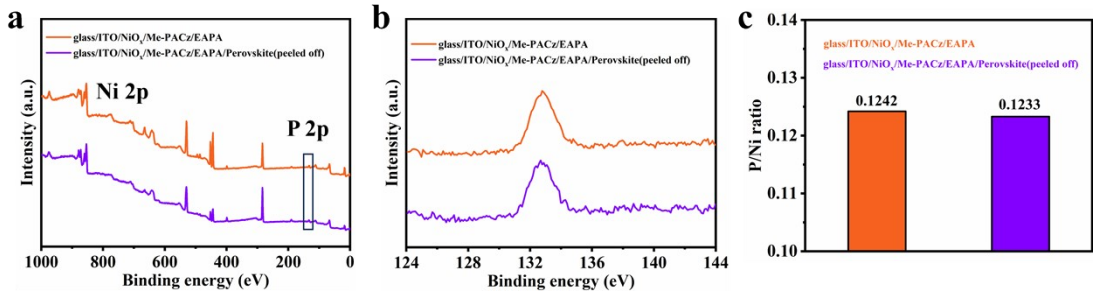

Fig. S10 (a) Survey XPS spectra, (b) P 2p XPS core spectra and (c) P/Ni ratio for the glass/ITO/NiO_x/Me-PACz/EAPA sample and glass/ITO/NiO_x/Me-PACz/EAPA/Perovskite(peeled off) samples, respectively.

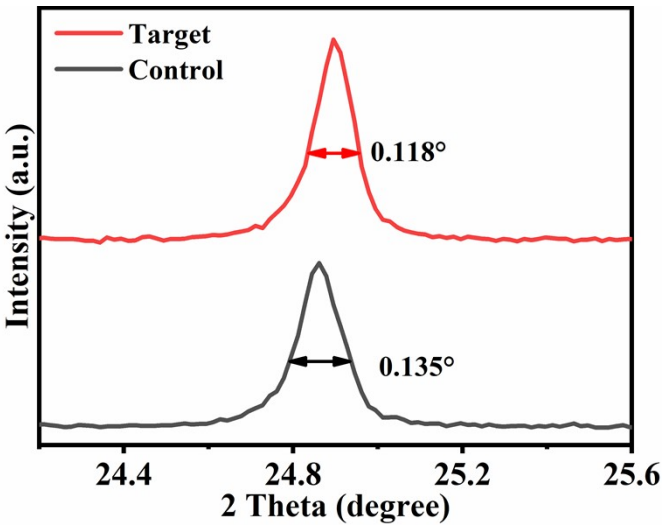

Fig. S11 FWHM of the (111) diffraction peak in the differently processed perovskite films.

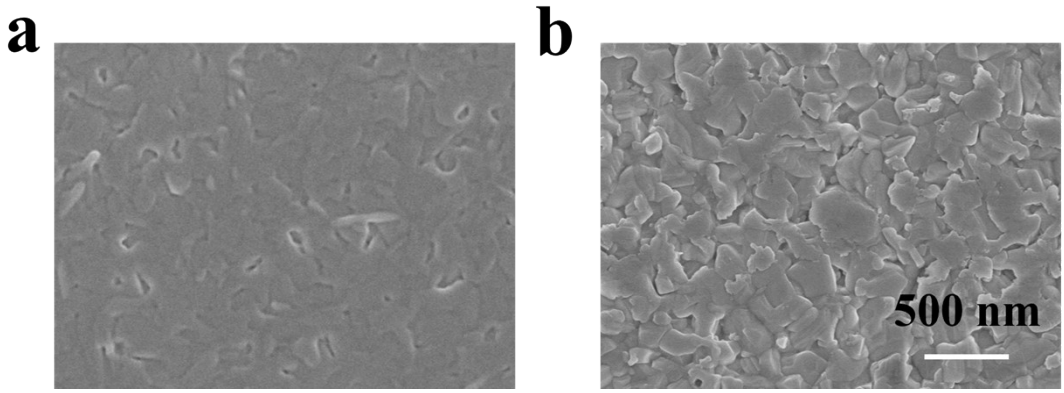

Fig. S12 The top SEM images of the PbI_2 (a) and PbI_2+EAPA (b) films.

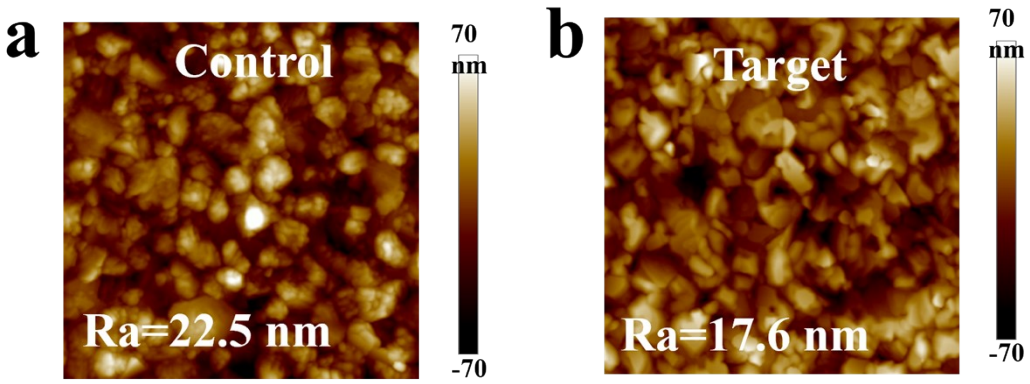

Fig. S13 The buried-view AFM images of Control and Target perovskite films (the scale bar is 10×10 um^2).

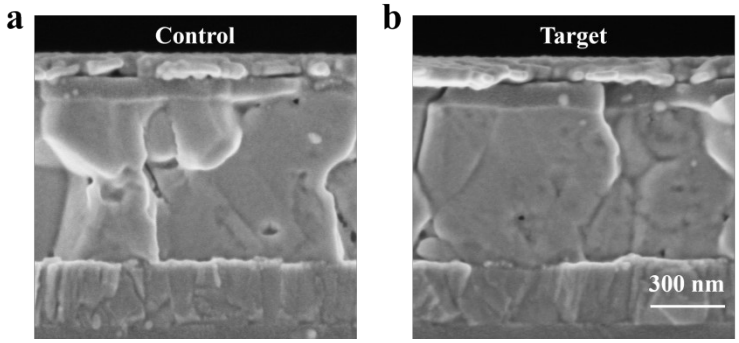

Fig. S14 The cross-sectional SEM images of the corresponding perovskite films.

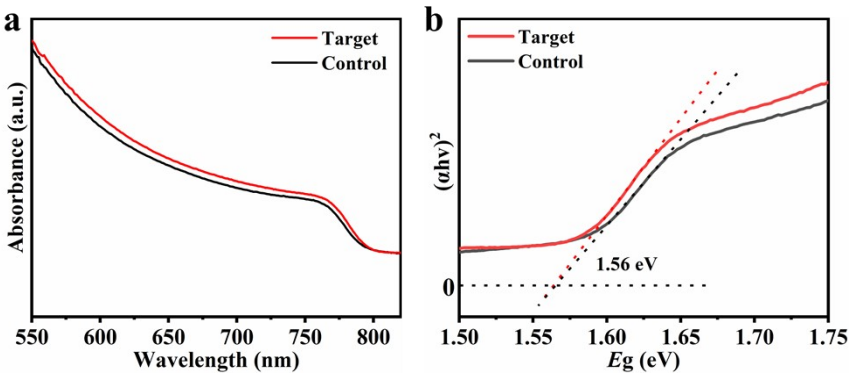

Fig. S15 (a) UV-vis absorption spectroscopy and (b) the optical bandgaps of differently processed perovskite films.

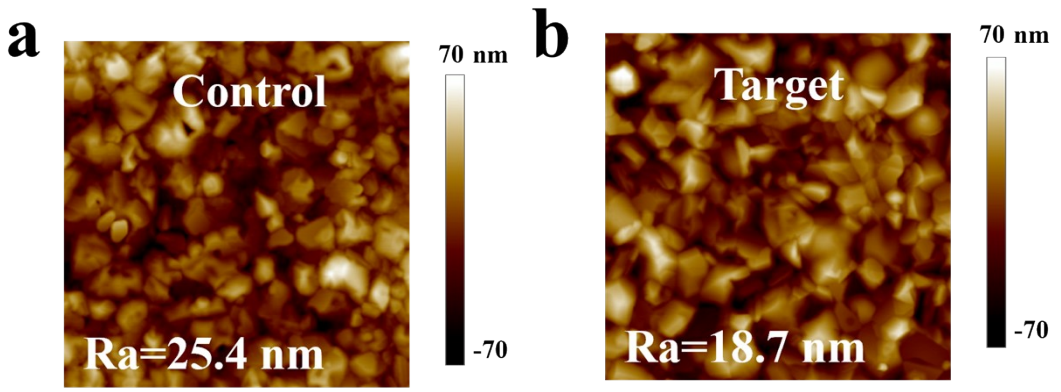

Fig. S16 The top-view AFM images of Control and Target perovskite films (the scale bar is 10×10 um^2).

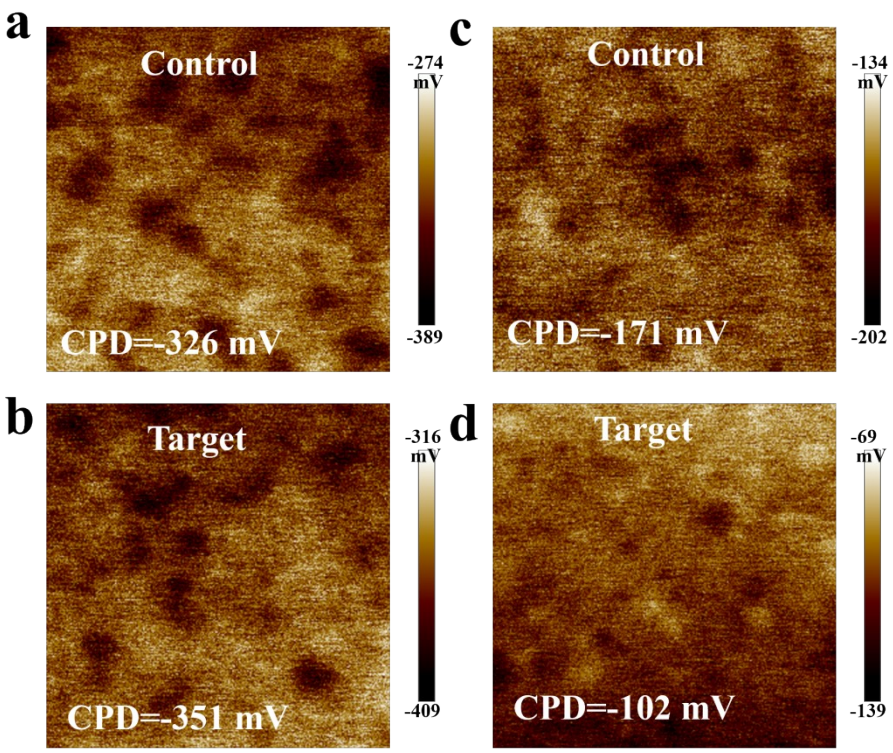

Fig. S17 The (a, b) buried interface and (c, d) top-view KPFM images of the corresponding perovskite films (10×10 um^2).

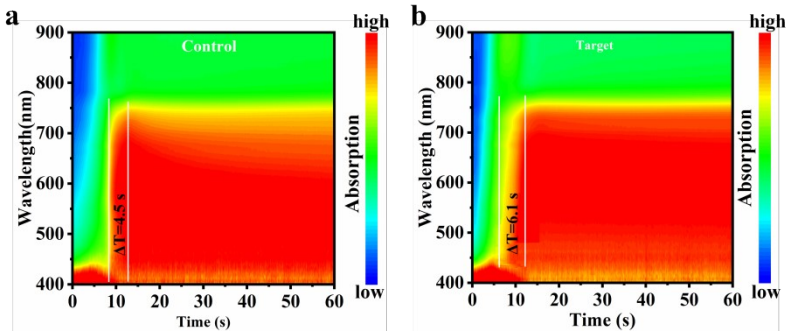

Fig. S18 In situ absorption spectra of the Control and Target films during the annealing stages.

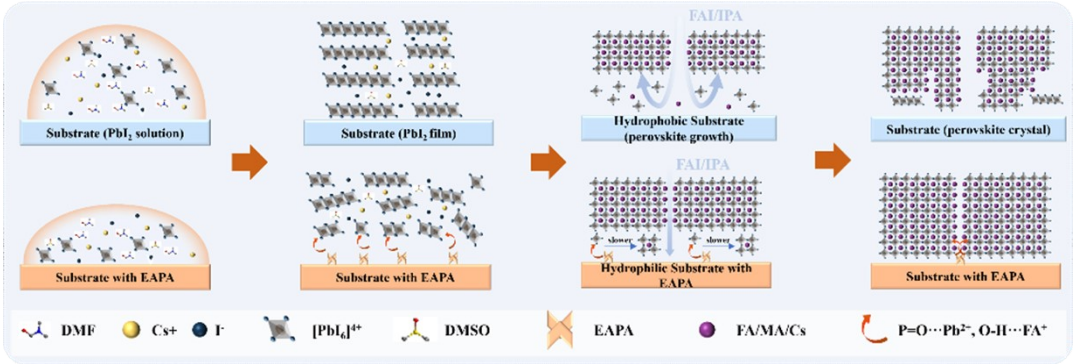

Fig. S19 The perovskite growth mechanism of Control (top) and Target (bottom) films managed by EAPA. And the substrate represents the double hole transport layer composed of NiO_x and Me-4PACz.

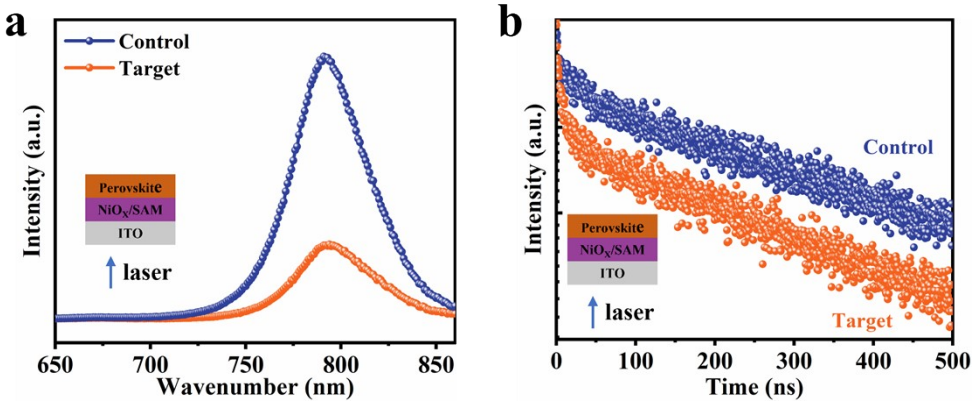

Fig. S20 (a) PL spectra and (b) TRPL spectra (based on ITO/NiO_x/SAM/perovskite structure).

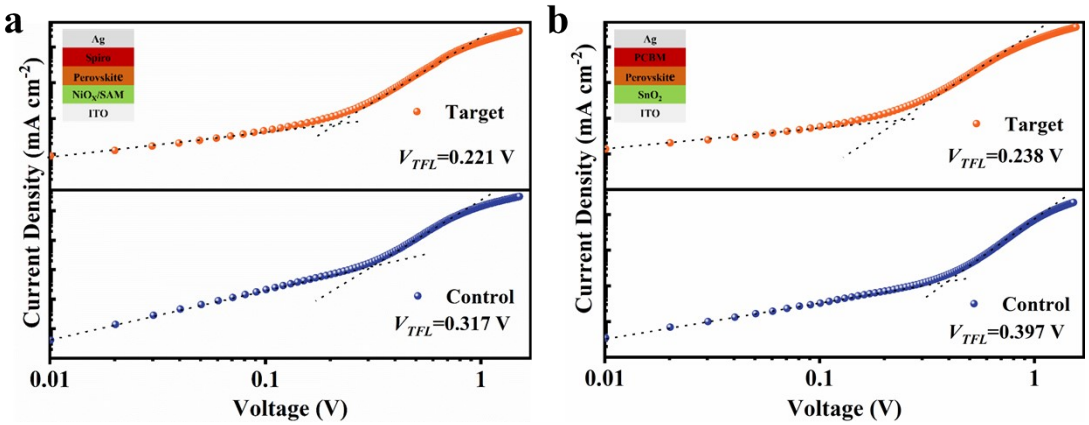

Fig. S21 Dark *J-V* curves of the (a) hole-only and (b) electron-only devices based on the Control and Target perovskite films.

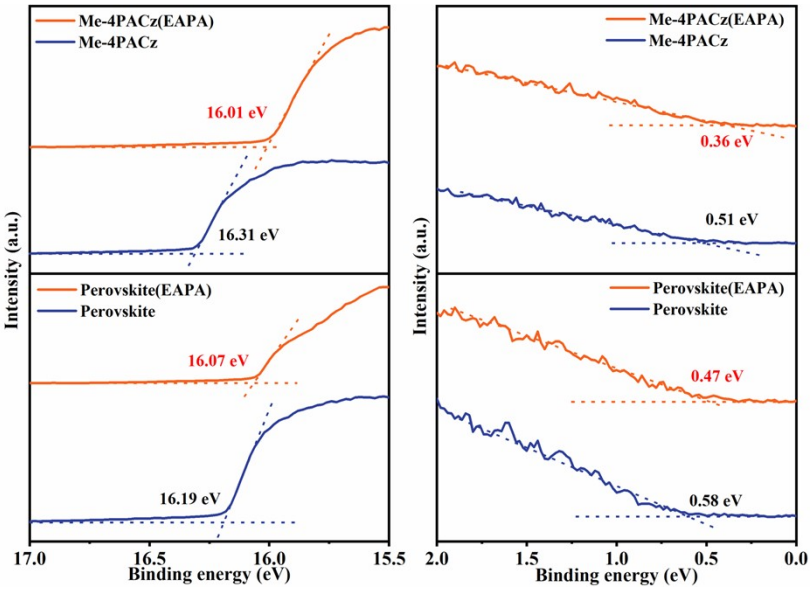

Fig. S22 Cut-off region and onset region of UPS for bare NiO_x/Me-4PACz and NiO_x/Me-4PACz/EAPA (top row), cut-off region and onset region of UPS for buried surfaces of the two types of perovskite films (bottom row).

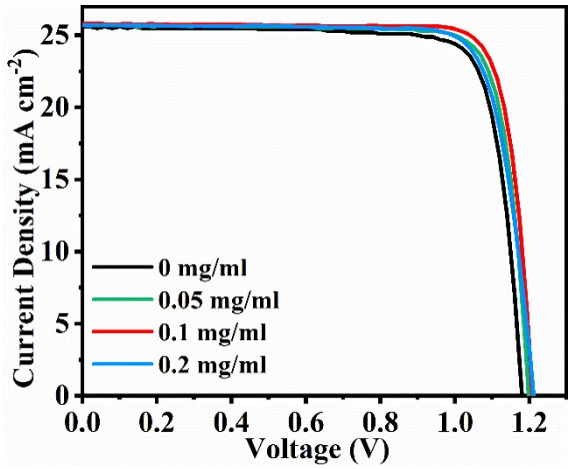

Fig. S23 *J-V* curves of the devices with various concentrations of EAPA.

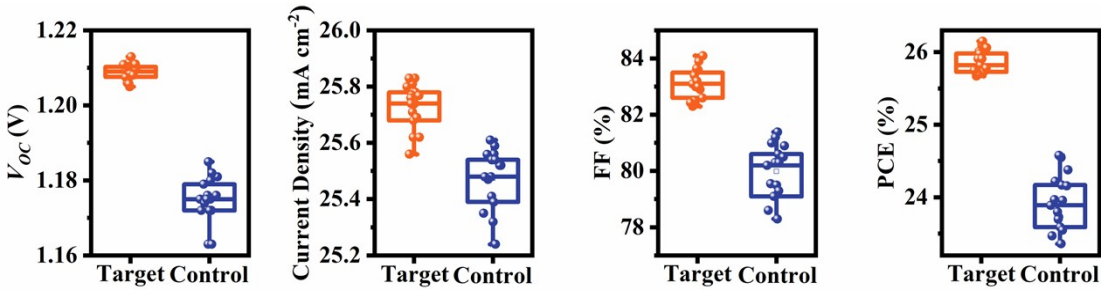

Fig. S24 The V_{OC}, J_{SC}, FF and PCE distributions for the different series of devices, statistics was calculated from 16 individual devices.

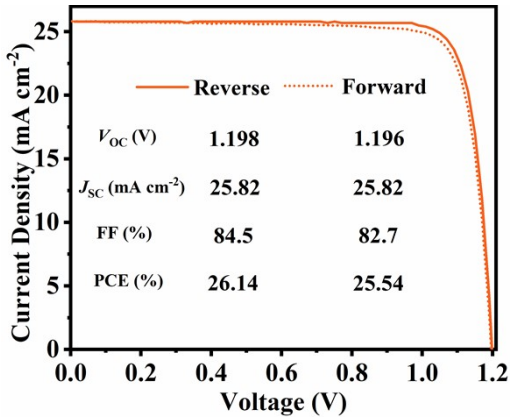

Fig. S25 The reverse (solid line) and forward (dotted line) sweep *J-V* curves of the best-performance devices of the repeated experiments conducted by Dr. Wei's group.

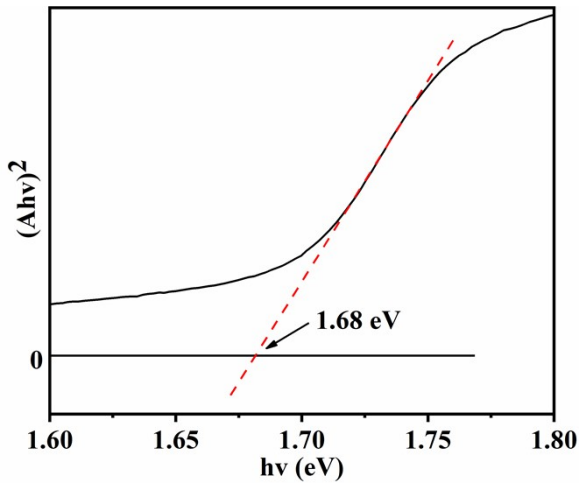

Fig. S26 The optical bandgaps of 1.68 eV perovskite films prepared by the two-step method.

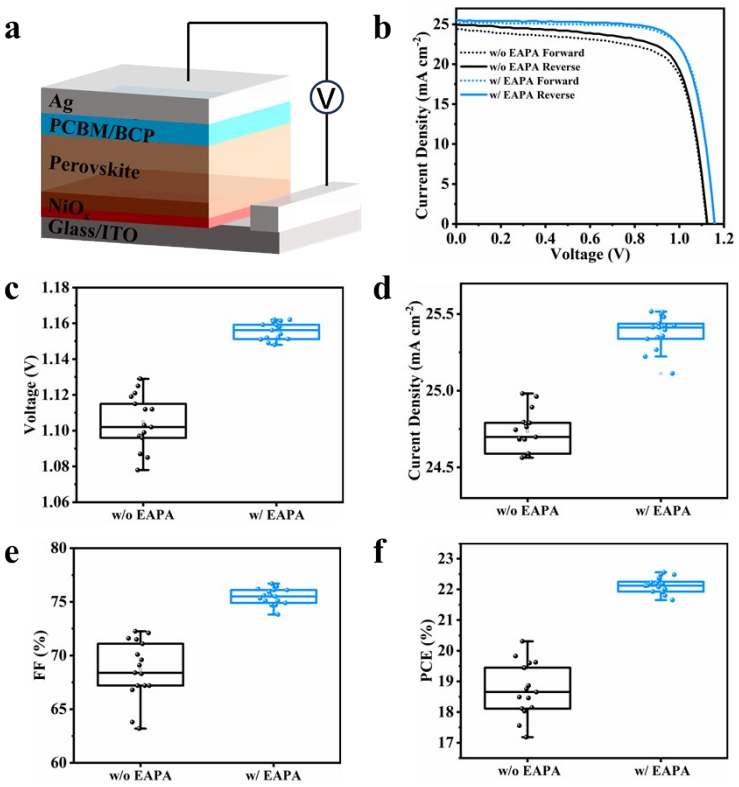

Fig. S27 (a) Schematic diagram of the inverted PSCs device structure by reinforced self-assembled molecular layer. (b) The reverse (solid line) and forward (dotted line) sweep *J-V* curves of the best-performance devices with the differently processed perovskite absorber films. The (c) V_{OC}, (d) J_{SC}, (e) FF and (f) PCE distributions for the different series of devices, statistics was calculated from 16 individual devices.

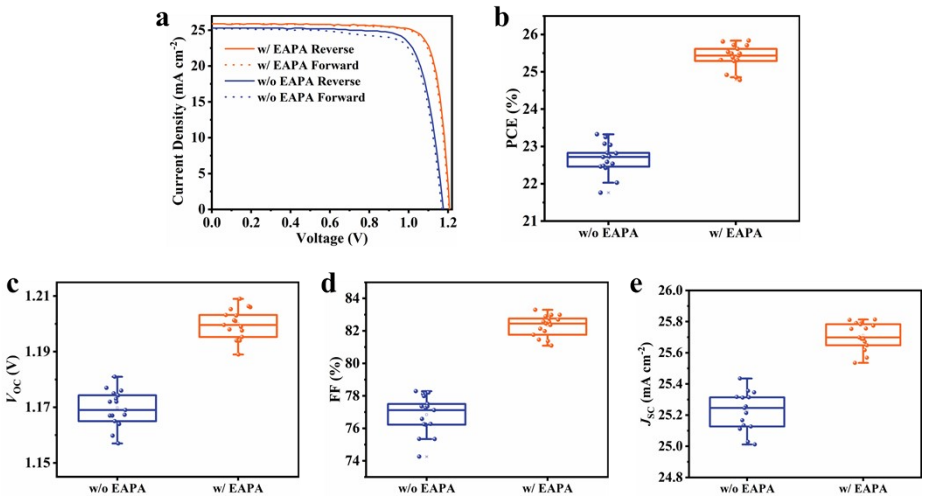

Fig. S28 (a) The reverse (solid line) and forward (dotted line) sweep *J*-*V* curves of the best-performance devices by using the blade-coating SAM method with the differently processed perovskite absorber films. The (b) PCE, (c) V_{OC}, (d) FF, and (e) J_{SC} distributions for the different series of devices, statistics was calculated from 16 individual devices.

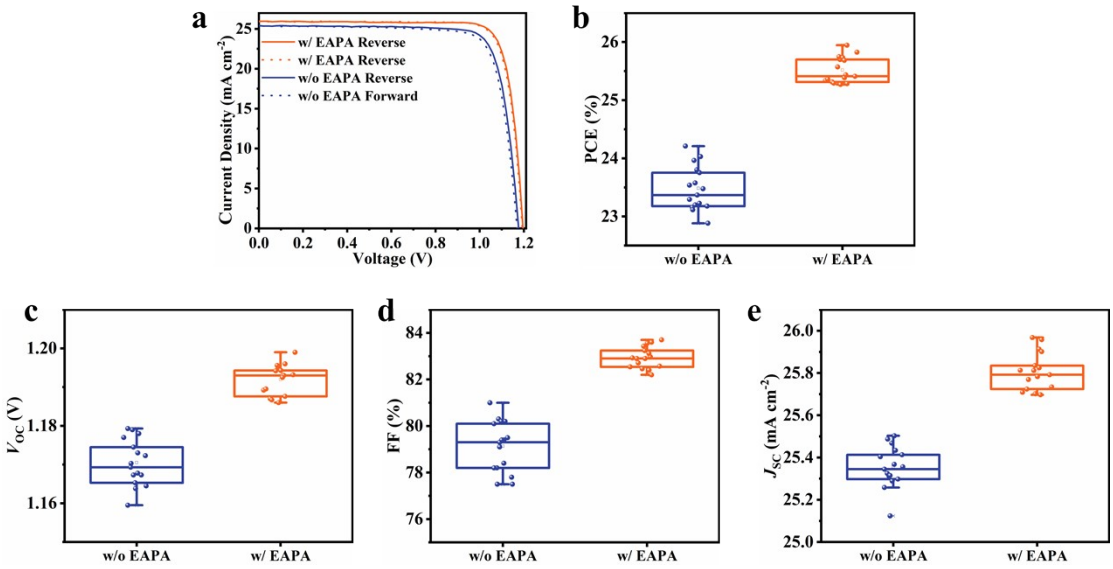

Fig. R29 (a) The reverse (solid line) and forward (dotted line) sweep *J-V* curves of the best-performance devices with the differently processed perovskite absorber films fabricated using the conventional antisolvent-assisted annealing method. The (b) PCE, (c) V_{OC}, (d) FF, and (e) J_{SC} distributions for the different series of devices, statistics was calculated from 16 individual devices.

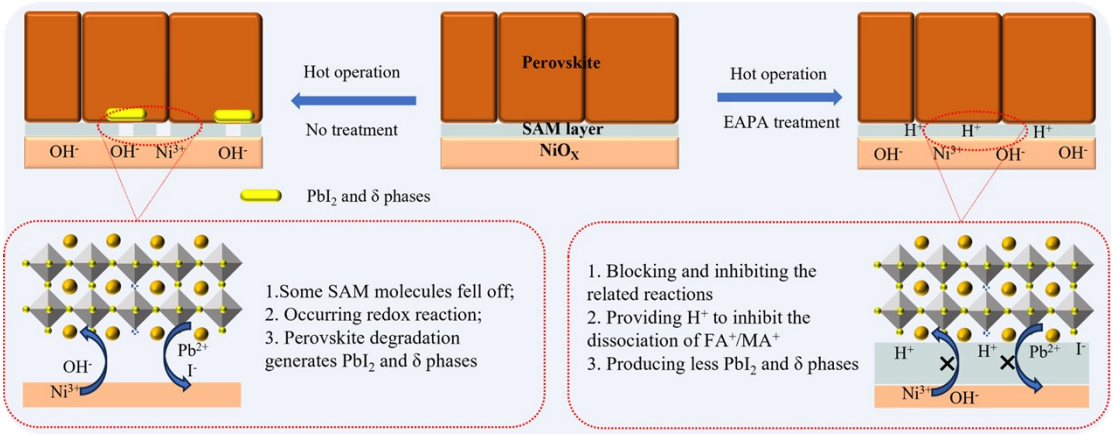

Fig. S30 Schematic diagram illustrating the stabilization of self-assembled molecular layer by EAPA to improve the stability of perovskite solar cells devices.

Table S1 The penetration depth of X-ray into perovksite film at different incident angles. The penetration depth (D) of X-rays in perovskite thin films at different incident angles is calculated by the formula: $D = \sin\alpha/\mu$, where α is the incident angle and μ is the attenuation coefficient.[25] At low incident angles, the depth is directly proportional to the α angle, and the approximate corresponding relationship is as follows.

Incident angle (°)	Approximate penetration depth (nm)
0.25	37
0.5	75
1	150
2	300
4	600

Table S2 TRPL decay fitting parameters for the buried interface of the control and EAPA treated perovskite films.

Samples	**A_1**	**τ_1(ns)**	**A_2**	**τ_2(ns)**	**τ_{ave} (ns)**
Control	0.112	36.23	0.888	649.09	644.82
Target	0.008	18.56	0.992	1845.12	1844.97

Table S3 Fast and slow components of the PL decay curves and their corresponding ratios for differently processed perovskite films.

Samples	**A_1**	**τ_1 (ns)**	**A_2**	**τ_2 (ns)**	**τ_{ave} (ns)**
Control	0.153	16.394	0.847	283.97	281.21
Target	0.556	6.208	0.444	196.34	189.10

Table S4 Measured PLQY values and calculated QFLS parameters.

Sample	PLQY (%)	QFLS (eV)
EAPA	6.432	1.231
PVK	3.891	1.218
HTL/EAPA	4.721	1.223
HTL/PVK	1.663	1.196

Table S5 Photovoltaic parameters extracted from *J-V* curves of the control and target PSCs under forward (FS) and reverse (RS) scans (refer to Fig. 5b).

	V_{oc} (V)	J_{sc} (mA cm^{-2})	FF (%)	PCE (%)
Control-RS	1.180	25.56	81.4	24.55
Control-FS	1.179	25.56	79.5	23.97
Target-RS	1.209	25.89	83.9	26.27
Target-FS	1.209	25.86	83.5	26.11

Table S6 A summary of the photovoltaic parameters reported in the literature related to inverted PSCs prepared by the two-step method. (refer to Fig. 5c)

Device structure	V_{OC} (V)	J_{SC} (mA cm^{-2})	FF (%)	PCE (%)	Ref.
ITO/MeO-2PACz/$Cs_yFA_{1-y}Pb(I_{1-x}Cl_x)_3$/PCBM/BCP/Ag	1.087	25.57	82.8	23	26
PEN/ITO/PTAA/Perovskite (1.52 eV)/C60/BCP/Ag	1.142	24.27	83.01	23	27
ITO/2PACz/Perovskite (1.56 eV)/PCBM/BCP/Ag	1.162	24.47	82.28	23.4	28
ITO/PTAA/$FAMAPbI_3$ (1.55 eV)/PCBM/BCP/Cu	1.13	25.2	82	23.4	29
ITO/Me-4PACz/Perovskite/C60/BCP/Ag	1.176	25.33	82.03	24.43	30
ITO/NiO_x/Me-4PACz/$FAMACsPbI_3$ (1.56 eV)/PCBM/BCP/Ag	1.188	25	83	24.6	31
ITO/SAMs/Perovskite (1.55 eV)/C60/BCP/Cu	1.173	25.15	83.8	24.72	32
ITO/NiO_x/2PACz/Perovskite (1.55 eV)/PCBM/BCP/Ag	1.14	26.19	83.52	25.05	33
ITO/Me-4PACz/$FA_{1-x}MA_xPbI_3$ (1.56 eV)/C60/BCP/Ag	1.173	25.78	83.08	25.12	34
ITO/NiO_x/Me-4PACz/$FA_{1-x}MA_xPbI_3$ (1.55 eV)/C60/BCP/Ag	1.2	25.95	82.29	25.59	35
ITO/NiO_x/Me-4PACz/$FAMACsPbI_3$ (1.54 eV)/PCBM/BCP/Ag	1.199	25.56	83.7	25.66	36
ITO/NiO_x/Me-2PACz/$FAMAPbI_3$ (1.55 eV)/C60/BCP/Ag	1.191	25.58	85.3	25.98	37
ITO/NiO_x/Perovakite (1.56 eV)/PCBM/BCP/Ag	1.201	26.17	83.73	26.32	38
ITO/NiO_x/Me-4PACz/$FAMACsPbI_3$ (1.56 eV)/PCBM/BCP/Ag	1.209	25.89	83.9	26.27	This work

Table S7 A summary of the performance of devices assembled using different concentrations of EAPA (statistics from 16 individual devices in each batch).

Samples (EAPA)		V_{OC} (V)	FF (%)	J_{sc} (mA cm^{-2})	PCE (%)
0	Average	1.175 ± 0.006	80.0 ± 1.0	25.47 ± 0.11	23.94±0.38
0.1 mg/ml	Average	1.209 ± 0.002	83.1 ± 0.5	25.73 ± 0.08	25.86±0.16

Table S8 Photovoltaic parameters extracted from *J-V* curves of the control and target wide-bandgap PSCs prepared by the two-step method under forward (FS) and reverse scan (RS) scans (refer to Fig. 5j).

	V_{oc} (V)	J_{sc} (mA cm^{-2})	FF (%)	PCE (%)
Control-RS	1.217	21.79	80.1	21.24
Control-FS	1.220	21.75	77.6	20.58
Target-RS	1.267	22.11	83.3	23.33
Target-FS	1.260	22.15	82.7	23.07

Table S9 Photovoltaic parameters extracted from *J-V* curves of the control and target PSCs under forward (FS) and reverse (RS) scans (refer to Fig. S27b).

	V_{oc} (V)	J_{sc} (mA cm^{-2})	FF (%)	PCE (%)
w/o EAPA-RS	1.125	24.98	72.3	20.31
w/o EAPA-FS	1.122	24.41	71.3	19.53
w/ EAPA-RS	1.158	25.48	76.4	22.56
w/ EAPA-FS	1.156	25.23	76.8	22.41

Table S10 Photovoltaic parameters extracted from *J-V* curves of the PSCs under forward (FS) and reverse (RS) scans (refer to Fig. S28a).

	V_{oc} (V)	J_{sc} (mA cm^{-2})	FF (%)	PCE (%)
w/o EAPA-RS	1.177	25.32	78.3	23.33
w/o EAPA-FS	1.168	25.18	77.0	22.63
w/ EAPA-RS	1.206	25.81	83.0	25.84
w/ EAPA-FS	1.204	25.90	81.8	25.51

Table S11 Photovoltaic parameters extracted from *J-V* curves of the PSCs under forward (FS) and reverse (RS) scans (refer to Fig. S29a).

	V_{oc} (V)	J_{sc} (mA cm^{-2})	FF (%)	PCE (%)
w/o EAPA-RS	1.177	25.40	81.0	24.211
w/o EAPA-FS	1.170	25.29	80.2	23.73
w/ EAPA-RS	1.196	25.96	83.6	25.95
w/ EAPA-FS	1.193	25.91	83.3	25.73

References

[1] Kresse, G. & Hafner, J. Ab initio molecular-dynamics simulation of the liquid-metalamorphous- semiconductor transition in germanium. Phys. Rev. B. 1994, 49, 14251–14269.

[2] Perdew, J. P., Burke, K. & Ernzerhof, M. Generalized gradient approximation made simple. Phys. Rev. Lett. 1996, 77, 3865–3868.

[3] Zur, A. & McGill, T. C. Lattice match: An application to heteroepitaxy. J. Appl. Phys. 1984, 55, 378–386.

[4] Jong, U. G., Yu, C. J., Kim, Y. S., Kye, Y. H. & Kim, C. H. First-principles study on the material properties of the inorganic perovskite $Rb_{1-x}Cs_xPbI_3$ for solar cell applications. Phys. Rev. B. 2018, 98, 32–39.

[5] Xue, H., Brocks, G. & Tao, S. First-principles calculations of defects in metal halide perovskites: A performance comparison of density functionals. Phys. Rev. Mater. 2021, 5, 125408.

[6] Cao, S. et al. Hybrid Self-Assembled Molecular Interlayers for Efficient and Stable Inverted Perovskite Solar Cells. Adv. Energy Mater. 2025, 15, 2405367.

[7] Płowaś-Korus, I. & Kaczkowski, J. Comparative density functional studies of $BiMO_3$ polymorphs (M = Al, Ga, In) based on LDA, GGA, and meta-GGA functionals. New J. Chem. 2022, 46, 15381–15391.

[8] Kresse, G. & Joubert, D. From ultrasoft pseudopotentials to the projector augmented-wave method. Phys. Rev. B. 1999, 59, 1758–1775.

[9] Blöchl, P. E. Projector augmented-wave method. Phys. Rev. B. 1994, 50, 17953–17979.

[10] Dudarev, S. L., Botton, G. A., Savrasov, S. Y., Humphreys, C. J. & Sutton, A. P. Electron-energy-loss spectra and the structural stability of nickel oxide: An LSDA+U study. Phys. Rev. B. 1998, 57, 1505–1509.

[11] Mohd Zaki, N. et al. Structural and electronic properties of nickel doped cobalt oxide electrode for supercapacitors: A first principle study. IOP Conf. Ser. Earth Environ. Sci. 2021, 685, 012029.

[12] Jain, A. et al. Commentary: The Materials Project: A materials genome approach to accelerating materials innovation. APL Mater. 2013, 1, 011002.

[13] Frisch, M. J. et al. Gaussian 16 Revision C.01. Gaussian 16, Revision C.01, Gaussian, Inc., Wallin (2016).

[14] LAMMPS - a flexible simulation tool for particle-based materials modeling at the atomic, meso, and continuum scales. Comput. Phys. Commun. 2022, 271, 108171.

[15] Dodda, L. S., Cabeza de Vaca, I., Tirado-Rives, J. & Jorgensen, W. L. LigParGen web server: an automatic OPLS-AA parameter generator for organic ligands. Nucleic Acids Res. 2017, 45, 331–336.

[16] Meltzer, C. et al. Indentation and self-healing mechanisms of a self-assembled monolayer--a combined experimental and modeling study. J. Am. Chem. Soc. 2014, 136, 10718–10727.

[17] Chirlian, L. E. & Francl, M. M. Atomic charges derived from electrostatic potentials: A detailed study. J. Comput. Chem. 1987, 8, 894–905.

[18] Ye, X., Cui, S., de Almeida, V. F. & Khomami, B. Effect of varying the 1–4 intramolecular scaling factor in atomistic simulations of long-chain N-alkanes with the OPLS-AA model. J. Mol. Model. 2013, 19, 1251–1258.

[19] Park, S. M. et al. Low-loss contacts on textured substrates for inverted perovskite solar cells. Nature. 2023, 624, 289–294.

[20] Hermawan, A. et al. Octahedral morphology of NiO with (111) facet synthesized from the transformation of NiOHCl for the NO_x detection and degradation: experiment and DFT calculation. Inorg. Chem. Front. 2020, 7, 3431–3442.

[21] Leonov, I. & Biermann, S. Electronic correlations at paramagnetic (001) and (110) NiO surfaces: Charge-transfer and Mott-Hubbard-type gaps at the surface and subsurface of (110) NiO. Phys. Rev. B. 2021, 103, 165108.

[22] A.M. Goodman, A. Rose, Double Extraction of Uniformly Generated Electron-Hole Pairs from Insulators with Noninjecting Contacts. Journal of Applied Physics. 1971, 42 (7), 2823-2830.

[23] X. Shi, Y. Ding, S. Zhou, B. Zhang, M. Cai, J. Yao, L. Hu, J. Wu, S. Dai, M.K. Nazeeruddin, Enhanced Interfacial Binding and Electron Extraction Using Boron-

Doped TiO_2 for Highly Efficient Hysteresis-Free Perovskite Solar Cells. Advanced Sciece. 2019, 6 (21), 1901213.

[24] M. Hao, Y. Zhou, Grain-boundary grooves in perovskite solar cells. Joule. 2024, 8 (4), 913-921.

[25] J. Cao, H.L. Loi, Y. Xu, X. Guo, N. Wang, C.k. Liu, T. Wang, H. Cheng, Y. Zhu, M.G. Li, W.Y. Wong, F. Yan, High-Performance Tin–Lead Mixed-Perovskite Solar Cells with Vertical Compositional Gradient. Advanced Materials. 2021, 34, 2107729.

[26] Y. Zheng, Z. Zhan, N. Pang, Y. Lu, Z. Lin, T. Shi, K. Chen, D. Lin, Y. Jiang, W. Xie, Gradient Doping for Stres-Relief in Vapor-deposited Perovskite Film to Achieve High-performance p-i-n Perovskite Solar Cells with a 23% Efficiency. Advanced Materials. 2025, 37 (28), 2501162.

[27] H. Zhang, Y. Bi, Y. Wang, C. Liu, N. Chen, J. Feng, Manipulating crystallization kinetics of perovskites by acetylsalicylic acid for efficient and stable two-step inverted flexible perovskite solar cells. Chemical Engineering Journal. 2025, 518, 164708.

[28] Q. Sun, S. Duan, G. Liu, X. Meng, D. Hu, J. Deng, B. Shen, B. Kang, S.R.P. Silva, Porous Lead Iodide Layer Promotes Organic Amine Salt Diffusion to Achieve High Performance p-i-n Flexible Perovskite Solar Cells. Advanced Energy Materials. 2023, 13 (36), 2301259.

[29] P. Chen, Y. Xiao, L. Li, L. Zhao, M. Yu, S. Li, J. Hu, B. Liu, Y. Yang, D. Luo, C.H. Hou, X. Guo, J.J. Shyue, Z.H. Lu, Q. Gong, H. J. Snaith, R. Zhu, Efficient Inverted Perovskite Solar Cells via Improved Sequential Deposition. Advanced Materials. 2022, 35 (5), 2206345.

[30] J. Fang, D. Lin, G. Xie, S. Li, H. Li, X. Wang, D. Wang, N. Huang, H. Peng, L. Gan, Y. Zhu, S. He, L. Qiu, Anion exchange promoting non-impurities enables conformable and efficient inverted perovskite solar cells. Energy & Environmental Science. 2024, 17 (20), 7829-7837.

[31] Y. Zheng, T. Zheng, S. Luo, H.A. Tauqeer, Y. Zhuo, S. Cao, Z. Bi, L. G. Gutsev, D. Liu, B. R. Ramachandran, G. L. Gutsev, A. S. Vasenko, O. V. Prezhdo, X. Xu, Complementary Molecular Passivation of Multiple Surface Defects for Efficient and Stable Inverted Perovskite Solar Cells. Small. 2025, 21 (39), e05659.

[32] J. Wang, Y. Zhou, W. Ai, D. Pu, H. Fang, S. Fu, H. Guan, W. Shao, G. Chen, W. Meng, G. Fang, W. Ke, Streamlined Phase Transition and Reaction Compensation in Hybrid Evaporation-Solution Deposited Inverted Perovskite Solar Cells. Advanced Energy Materials. 2024, 15 (15), 2404954.

[33] G. Wu, J. Wang, X. Fang, J. Xu, X. Xia, J. Zhao, L. Zheng, M. Zhang, Z. Chen, H. Chen, L. Wang, W.W. Yu, Two-Step Inverted Perovskite Solar Cells with > 25% Efficiency Fabricated in Ambient Air. Advanced Energy Materials. 2025, 15 (27), 2500830.

[34] D. Qu, C. Shang, X. Yang, C. Wang, B. Zhou, Q. Qin, L. Gao, J. Qiao, Q. Guo, W. Yang, K. Wang, R. Zhu, Y. Tu, W. Huang, Phase homogeneity mediated charge-carrier balance in two-step-method halide perovskite photovoltaics. Energy & Environmental Science. 2025, 18 (3), 1310-1319.

[35] C. Xu, P. Hang, C. Kan, X. Guo, X. Song, C. Xu, G. You, W.-Q. Liao, H. Zhu, D. Wang, Q. Chen, Z. Hong, R.-G. Xiong, X. Yu, L. Zuo, H. Chen, Molecular ferroelectric self-assembled interlayer for efficient perovskite solar cells. Nature Communications. 2025, 16 (1), 835.

[36] S. Luo, S. Cao, T. Zheng, Z. Bi, Y. Zheng, Y. Li, B.Z. Taye, V.V. Ozerova, L.A. Frolova, N.A. Emelianov, E.D. Tarasov, Z. Liang, L.G. Gutsev, S.M. Aldoshin, B.R. Ramachandran, P.A. Troshin, X. Xu, Melamine holding PbI_2 with three “arms”: an effective chelation strategy to control the lead iodide to perovskite conversion for inverted perovskite solar cells. Energy & Environmental Science. 2025, 18 (5), 2436-2451.

[37] Z. Gao, J. Kou, W. Lv, Y. Chen, L. Ren, P. Huang, Tailoring self-assembled monolayers with post-assembly nicotinic acids for efficient and ultraviolet stable inverted perovskite solar cells. Journal of Materials Chemistry A. 2025, 13 (38), 32290-32299.

[38] M. Tao, Y. Wang, K. Zhang, Z. Song, Y. Lan, H. Guo, L. Guo, X. Zhang, J. Wei, D. Cao, Y. Song, Molecule-triggered strain regulation and interfacial passivation for efficient inverted perovskite solar cells. Joule. 2024, 8 (11), 3142-3152.